ADVANCED INTELLIGENT SYSTEMS Open Access
www.advintellsyst.com

Origami-Patterned Rigidification for Soft Robotic Bifurcation

Dihan Liu, Sicong Liu, Wenjian Yang, Juan Yi, Hongqiang Wang, Wenzeng Zhang, Jian S. Dai,* and Zheng Wang*

The fluid-transportation functions based on the volume-regulating behavior of the chamber-like organs inspire the development of artificial organs. Due to the intrinsic compliance of soft robotics for biomimicking purposes and the volume-regulation capability of the 3D origami patterns, the soft robots with origami patterns show promising potential in such research. However, the folding deformation of the origami facets cannot be straightforwardly implemented as the actuation or the body movement, and the predetermined movements of the pattern limit the appropriate functions for specific applications. In this work, an origami-patterned rigidification (OPR) method is proposed for applying rigid origami mechanisms (herein, the cuboctahedron origami ball) to the chamber-like structure of soft robots. The motion of the soft robot is programmed by purposefully rigidified the soft chamber following the pattern. The resultant OPR structures are granted with functions corresponding to the predetermined motion of the pattern, and the expanded movements through the bifurcation brought by the soft–rigid characteristics. The concept, design, and fabrication of the OPR robot are presented. By analyzing the deformation of the soft creases, the kinematic models of the predetermined and expanded degrees of freedom are presented and verified by experiments. The extended functions of two OPR robots are demonstrated.

1. Introduction

Organs such as the heart in the circulatory system, stomach in the digestive system, and lungs in the respiratory system share a chamber-like profile and transport fluid in desired directions by the volume change driven by a combination of muscular movements, as shown in **Figure 1**a.

The stomach, in particular, works in multiple directions, which can transport food to the intestines and squeeze out food to cause vomiting.[1] Artificial organs are proposed to mimic the volume-regulating function with the chambers,[2–4] using multiple degree-of-freedom (DOF) movements driven by different sets of muscles. Artificial organs with membranes or cavities made of flexible materials have advantages in simulating the function of muscles and body tissues due to intrinsic compliance, thereby simulating biological rhythms.[5,6]

Soft actuators are commonly applied in bioinspired robots.[7] Integrating soft actuators and chambers in soft robotics enables the function simulation of muscles for the chamber movements inspired by the organs, which differ from the combination of independent rotations or translations in rigid mechanisms. The soft pumps simulate the control of blood flow by the calf muscle.[8] The chamber-shaped robots simulate the locomotor organs of squid.[9,10] The fluid conveyed by these robots exhibits a unidirectional flow without focusing on transporting in the desired directions.

Origami is a flexible mechanism with customizable characteristics that can transform from 2D shapes to 3D structures and continue to deform in 3D space.[11] The existing origami mechanism has been favored by researchers, especially in the field of soft robots, which has been enthusiastically sought after,[12,13] including origami actuators,[14–16] robot arms,[17–20] worm robots,[21–23] soft grippers,[24,25] etc. The combination of origami and soft robots enforces the regularity of deformations and helps to enlarge the number of motions.

Due to the volume-regulation effect during the deformation of the 3D origami patterns, origami-patterned soft robots are developed with fluid-transportation capability. To push water out for propulsion, the origami chamber of the soft robot uses a motor to drive the parallel panel and contract the origami body to reduce volume.[26] A rope-driven actuation elongates or contracts the origami structure as an air pump.[27] For working as pure paper robots, the origami structures are made up of soft materials with properties similar to paper.[28,29] The incorporation of origami configuration into the chamber structure

D. Liu, S. Liu, W. Yang, J. Yi, H. Wang, J. S. Dai, Z. Wang
Department of Mechanical and Energy Engineering
Southern University of Science and Technology
Shenzhen 518000, China
E-mail: daijs@sustech.edu.cn; zheng.wang@ieee.org

W. Zhang
Department of Mechanical Engineering
Tsinghua University
Beijing 100084, China

The ORCID identification number(s) for the author(s) of this article can be found under https://doi.org/10.1002/aisy.202300767.

DOI: 10.1002/aisy.202300767

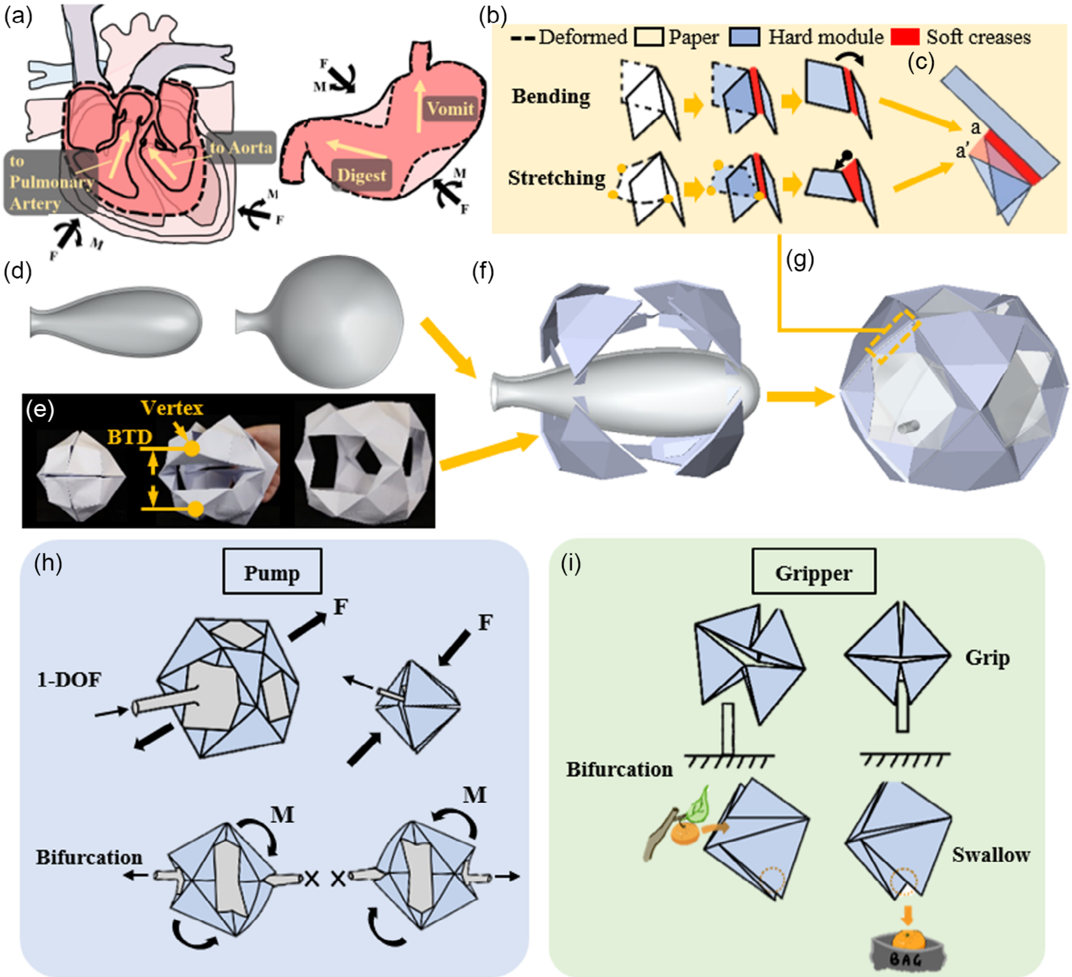

Figure 1. Concept of Origami-patterned-rigidification. a) Multi-DOF movements of the fluid-transporting organs are driven by combined movements of muscles. b) Bending and stretching properties of compliant material attached with hard modules. c) Bifurcation effect of soft creases with stretching and bending deformations. d) Inflation and deflation of uniform thickness soft chamber. e) The 1-DOF transformation of the cuboctahedron rigid origami ball. f) Combination of the hard modules extracted from the origami ball and soft chamber. g) The rigidified sphere-shaped OPR structure. h) Predetermined motion and bifurcation of the soft–rigid OPR structure and application as a pump. i) Application for OPR soft robots as a multifunctional gripper with grip and swallow modes.

imparts a greater degree of regularity to the deformation of the chamber.

For generating innovative functions of robots, mechanisms inspired by origami use bifurcation to expand the predetermined motion of the rigid origami pattern to a variety of movements. Wang et al.[30] provide a kinematotropic metamorphic mechanism that is reconfigurable and can bifurcate into multiple structures. The robot consists of such mechanism that can crawl over various terrains and conquer challenging obstacles with enhanced locomotivity.[31] Bifurcation provides such a mechanism with new possibilities, but it is yet to be applied to soft robots with origami structures for volume regulation. The soft–rigid structures enable the realization of functionality akin to bifurcation, thereby assisting robots in expanding their DOFs. Mintchev et al.[32] provide the bioinspired dual-stiffness robot that uses highly elastic materials and the extendable property to generate compliance when overloaded or impacted and returns to its original status when the external force disappears. Faber et al.[33] defined the stretching and rotation effects of creases and used the energy generated by the material during unfolding to achieve rapid folding or maintain a specific stable state. In recent years, theoretical studies have been presented on the energy stored by elastic materials that investigate the characteristics of soft creases.[34,35] However, few paradigms are available to design and exploit the movements of the soft chamber with origami patterns for practical soft robotic applications.

There are structures in existing works that combine hard modules with soft chambers, designed as a robotic arm[36] or actuators for neurosurgical brain retraction applications.[37] Zhang et al.[38] expand the DOF of the Kresling origami unit by adding rigid shells to the pneumatic chamber on the side of the origami unit. Soft chambers are combined with springs to reinforce the linearity of the chamber.[39] However, the DOF of a single chamber in these works is singular, and the soft–rigid chambers are driven by fluid. The deformation of the chambers or the fluid in them cannot be actively regulated with the rigid modules. Robots utilizing chambers have employed their chambers to grasp delicate marine organisms.[40,41] However, their functionality is constrained by the singular DOF of the rigid origami mechanism.

To fully utilize the folding movements of origami for the benefit of soft robots and extend the functionality for the rigid origami pattern, we propose an origami-patterned rigidification (OPR) method that adds preferable hard origami modules to the soft chamber, which forms a soft–rigid structure and achieves the direct application of origami mechanism to the chamber of soft robots. By innovatively driving the rigid panels using external soft actuators, the robot's movement is expanded from the predetermined origami DOF through the bifurcation brought by the soft–rigid characteristics of the OPR structure. The contributions are as follows.

First, the OPR method to rigidify the soft robotic chamber following the rigid origami pattern for compliant deformation programming is proposed. The rigid panels are actively driven by multiple sets of external soft actuators to simultaneously obtain the predetermined origami motion and generate new movements using bifurcation of the soft–rigid structure for added functionality.

Second, the predetermined and expanded movements are modeled by analyzing the deformations of the soft material between the rigidified areas, i.e., the soft creases. The experimental results of the Ori-1DOF and OPR Exp-DOF movements validated the models.

Third, enabled by the Exp-DOF movements, two soft robotic demonstrations are presented, including a multifunctional gripper, which works in both desktop and underwater environments and a valve-integrated fluid pump, which validates the practicality of the method.

The rest of this article is organized as follows. Section 2 presents the OPR concept and implements it with the cuboctahedron origami ball. Section 3 presents the design, fabrication, and modeling of the OPR structure. Section 4 introduces the actuation and control of the OPR robots. Demonstrations of two OPR soft robots are presented in Section 5. Section 6 concludes this article.

2. Concept of OPR

To realize multi-DOF movements inspired by the fluid-transporting organs as shown in Figure 1a, an origami mechanism is chosen to generate the volume regulation motions on the soft chamber. As shown in Figure 1d, a uniform-thickness soft chamber inflates into a sphere when subjected to fluidic pressure. The accurate control of expansion and directional volume regulation is difficult due to the hyper-elastic deformation of the compliant material used. Thus, a cuboctahedron rigid origami ball mechanism is selected to implement the folding behavior onto the soft chamber, as shown in Figure 1e. The 1-DOF rigid origami ball transforms from a closed sphere to a six-sided open truncated cubic octahedron,[42] whose polyhedral skeleton is the assembly of two Bennett linkages with triangular links and transforms with centrosymmetric in 3D space. During the transformation, there are identical beak-like openings on the six sides with the same beak-tip distance (BTD).

To achieve volume-regulation motion, hard modules following the rigid origami pattern are directly attached to the hyperelastic chamber to gain OPR. The hard modules are divided based on the rigid origami skeleton of the cuboctahedron origami ball. Eight identical large equilateral triangular hard modules (LETM) and 48 small right-angled triangular modules (SRTM) connected between the LETMs are extracted as shown in Figure 1f. All the hard modules are stuck directly on the surface of the hyperelastic chamber. The rigidified sphere-shaped OPR structure is shown in Figure 1g. The edges of the hard modules are parallel and spaced the same distance, and the compliant material in between forms the soft creases as shown in Figure 1b.

After rigidification, when a pair of forces are applied to the opposite LETMs to translate them away from each other, as shown in Figure 1h, the OPR structure obtains the predetermined movement of the origami pattern transforming from an octahedron to a cuboctahedron structure with the soft creases bend (Figure 1b), i.e., the Ori-1DOF movement.

When rotating the LETM, the soft–rigid OPR structure starts to bifurcate as shown in Figure 1h. The adjacent edges of the hard modules will not be parallel after bifurcation but are similar to the change of edge a to a', as shown in Figure 1c, with the soft creases stretching and bending (Figure 1b). The creases between the driving LETM and the adjacent LETM obtain the largest deformations than the others. Therefore, applying different rotations to the LETMs can lead to asymmetric changes in the OPR ball and result in six different BTDs. These expanded multiple movements are called the Exp-DOF movements.

To retain the ability to bend and stretch, the soft chamber should be made of hyperelastic materials such as silicone, rubber, thermoplastic polyurethane, etc. As long as the rigidified areas on the soft material follow the origami pattern, the hard modules can be of various thicknesses and shapes. Thus, connecting the hard modules to the driving units is convenient. To achieve motion control straightforwardly, two types of driving units are adopted for the Ori-1DOF movement and Exp-DOF movements, respectively. The combined actuation of driving units drives the rigid origami panels purposefully and generates desired motions for controlling the movements of the OPR structure. The combination of Ori-1DOF movement and Exp-DOF movement can bring new applications for OPR soft robots, such as the fluid-driven pump in Figure 1h and the multifunctional gripper in Figure 1i.

3. Implementation of OPR

3.1. Design and Fabrication of OPR Structure

The design of the LETM in the top view is shown in **Figure 2**a. To avoid interference at the folded status, the SRTMs are cut into two halves as shown in Figure 2b. The upper and lower halves are connected with two LETMs on different sides as shown in Figure 2c. Gaps with widths of C between the adjacent parallel edges are designed to allow the soft creases to deform. The parameters are noted in Figure 2a–c, and the values are

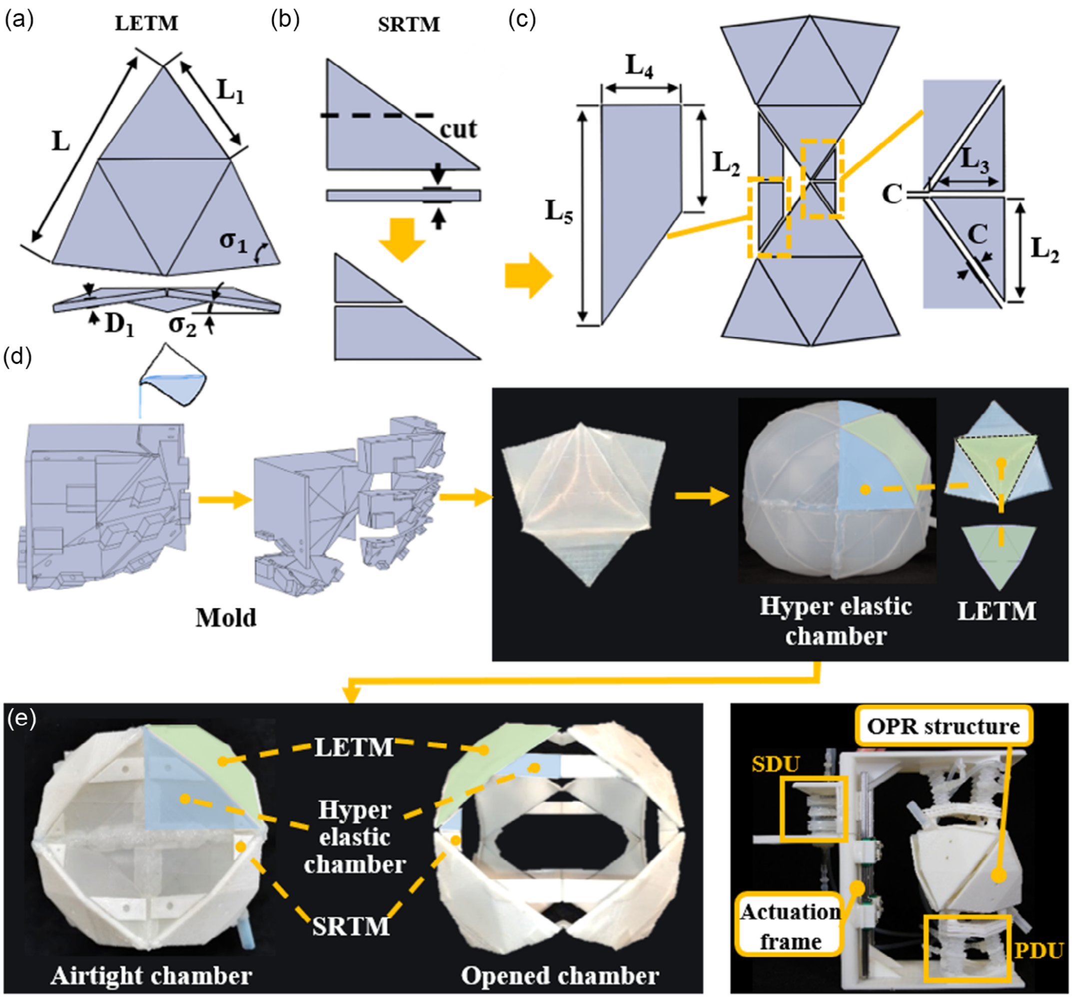

Figure 2. Design and fabrication of OPR structure. a) Side and top views of the LETM. b) Side and top views and division of the SRTM. c) Connection of LETMs with different parts of SRTMs. d) The manufacturing process of the soft–rigid OPR structure. e) OPR structures with airtight and opened chambers. f) External actuation of the OPR structure consists of two types of driving units: the series-driving unit (SDU) and the parallel-driving unit (PDU).

presented in **Table 1**. L_i, D_i, and σ_i refer to the length of the edge, the thickness, and the angle of LETM, respectively.

The hyperelastic chamber is manufactured of silicone Ecoflex30 (Smooth-On Inc., 1:1 proportion) by injection molding. According to the centrosymmetric structure of the origami ball, the identical one-eighth structure is used as a unit to design the molds as shown in Figure 2d. Eight identical silicone soft skins are obtained, assembled, and glued (E43, Wacker Inc.) to form an airtight chamber with uniform compliance. Two hole-shaped openings are arranged on the silicone ball's square area, allowing fluid to enter and exit. The hard modules are prepared by fused deposition modeling (FDM) 3D printing with polylactic acid (PLA) material (1.75 mm, white, Raised 3D Inc.). To maintain adequate stiffness, the thickness of an LETM is 3 mm. To keep the function of the creases and avoid interference in folding, the thickness of an SRTM is 1 mm. The hard modules and the soft chamber are glued together as shown in Figure 2d with silicone instant adhesive glue (6068, Aoxinda Inc.). Apart from the airtight chamber, by removing the silicone in the non-crease area and keeping the soft creases, the OPR structure is formed with six opened sides as shown in Figure 2e.

To generate deformations of the OPR structure, the actuation frame is designed and assembled on the OPR structure as shown in Figure 2f. The actuation frame has upper and lower parts connected by guide rails to output linear motion. The linear motion is driven by two axial translation pneumatic bellows in series, forming a series-driving unit (SDU). It is connected to the panels protruding from the left side of the actuation frame. The LETMs

Table 1. Design parameters of OPR structure.

Name	Value [mm]	Name	Value
L	89	C	1 mm
L_1	45	σ_1	7.93°
L_2	16.23	σ_2	70.52°
L_3	11.47	D_1	3 mm
L_4	12.6	D_2	1 mm
L_5	34.68	–	–

of the OPR structure are connected by three parallel arranged pneumatic soft origami actuators (SOAs),[43] which form the parallel-driving unit (PDU). Each of the two centrosymmetric and parallel-driving LETMs is connected to a PDU. The other ends of the PDUs are connected with the actuating frame as shown in Figure 2f.

3.2. Modeling of Ori-1DOF Movement

The coordinate system is established for theoretical analysis, as shown in **Figure 3**a. To facilitate the comparison between the experimental and the theoretical value, we select the twist angle ω which describes the variation of the normal vector on plane B as the output value as shown in Figure 3c.

During Ori-1DOF movement of the origami ball, the vertices of the LETMs remain on the planes of the coordinate system.[42] Let $a_1 = (a_{1x}, a_{1y}, a_{1z})^{\mathrm{T}}$, $b_1 = (b_{1x}, b_{1y}, b_{1z})^{\mathrm{T}}$, and $c_1 = (c_{1x}, c_{1y}, c_{1z})^{\mathrm{T}}$. Considering the motion of plate A which has the plane-symmetric relationship respect to the three coordinate planes, there are relationships between $|c_{1z}| = |a_{1x}| = |b_{1y}|$ and $|c_{1x}| = |a_{1y}| = |b_{1z}|$. Thus, the vertices of the panel can be expressed as $a_1 = (m, n, 0)^{\mathrm{T}}$, $b_1 = (0, m, n)^{\mathrm{T}}$, and $c_1 = (n, 0, m)^{\mathrm{T}}$, where m and n are coefficients of the distance between the vertices and the origin O as shown in Figure 3b. Note that the variable length of the LETM is L. Due to the movement restriction of the origami ball, m and $n \in \left(0, \frac{\sqrt{2}}{2}L\right)$. At a certain state in the process of motion, the value of n is given, m can be determined by the $|ab| = L$. In such way, the coordinates of the vertices at the deformed state can be calculated. Thus, the normal vector of the panel on the driving LETM is $\mathbf{n}_A = \mathbf{n}_{A'} = c_1a_1 \times c_1b_1$. The normal vector of the adjacent LETM plane B is $\mathbf{n}_{B'}$, which can be obtained due to plate A and B are symmetric about plane XOZ. The distance d between the centrosymmetric driving LETMs consists of the distance from the origin to the two plates, which can be calculated as

$$d = 2\frac{\mathbf{c_1O} \cdot \mathbf{n}_{A'}}{|\mathbf{n}_{A'}|} \tag{1}$$

If the center of the origami ball is fixed, each plate rotates around its normal vector during the Ori-1DOF movement, while the directions of the normal vectors are unchanged as shown in the assumed expansion state in Figure 3b. However, when driven by the SDU in the actuation frame as shown in Figure 3d, the normal vector of plate A remains unchanged during the translation of plate A, while normal vectors of the other plates change in the coordinate system. Thus, the green plate A' in Figure 3b needs to rotate angle φ around $\mathbf{n}_{A'}$ to reach the final position with

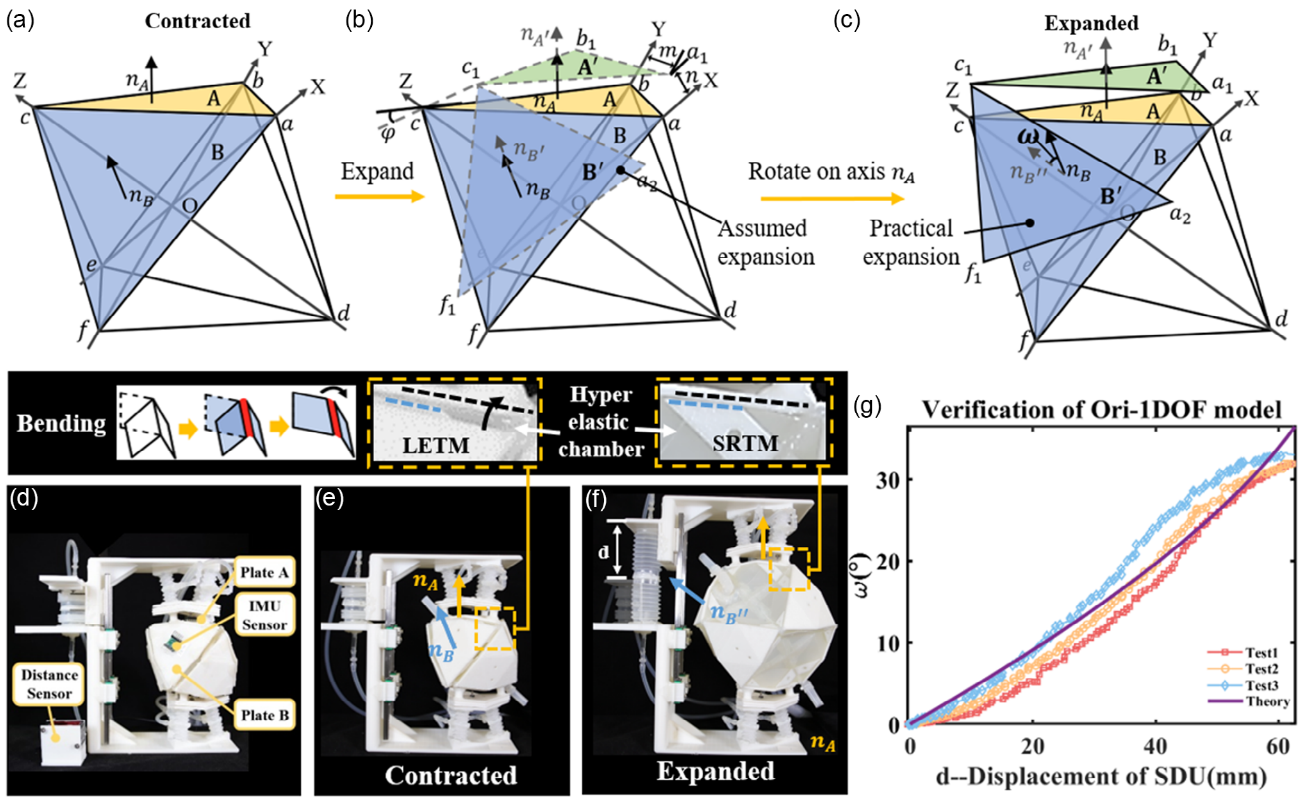

Figure 3. Modeling and verification of the predetermined movement Ori-1DOF. a) The schematic and established coordinate system of Ori-1DOF movement. b) The assumed plane-symmetric expansion with normal vectors unchanged for calculation. c) Practical expansion of Ori-1DOF movement with plate A translates in the direction of the normal vector. d) Experiment setup for Ori-1DOF movement validation. e) Contracted state of the structure and the details of the bending deformation at soft creases. f) Expanded state of the structure. g) Experiment and theoretical relationship of the input displacement and the twist angle in the Ori-1DOF movement.

no rotation relative to the yellow plate A in Figure 3c. Since A and A' are always parallel, the rotation angle

$$\varphi = \arccos\left(\frac{bc \cdot b_1c_1}{|bc||b_1c_1|}\right) \tag{2}$$

Taking the normal vector $\mathbf{n}_{A'} = [\mathbf{n}_a, \mathbf{n}_b, \mathbf{n}_c]^{\mathrm{T}}$ as the rotation axis of the origami ball in the world coordinate system, the rotation matrix can be obtained by Euler–Rodrigues formula.[44]

$$\boldsymbol{R}_1 = \mathrm{Rot}(\mathbf{n}_{A'}, \varphi) \tag{3}$$

Thus, the normal vector of the plate B after expansion is

$$\mathbf{n}_{B''} = \boldsymbol{R}_1 \cdot \mathbf{n}_{B'} \tag{4}$$

As shown in Figure 3c, A' in the expended state only translate relative to A at the initial state. $\mathbf{n}_{B''}$ and $\mathbf{n}_{B'}$ form the rotation angle of plane B which is calculated as

$$\omega = \arccos\left(\frac{\mathbf{n}_{B''} \cdot \mathbf{n}_{B'}}{|\mathbf{n}_{B''}||\mathbf{n}_{B'}|}\right) \tag{5}$$

Using Equation (1)–(5), the relationship between the twist angle can be derived.

To validate the model, an experiment on the 1-DOF expansion is carried out in the setup as shown in Figure 3d; a laser distance sensor (HG-C1200, Panasonic Inc.) is used to measure the displacement of the SDU, i.e., the relative displacement between the driving LETMs. The rotation of plate B is measured by the IMU sensor (JY61P, Witmotion Inc.) on the LETM module B. The experiments were performed three times; the contracted and expanded states of the OPR robot are shown in Figure 3e,f, respectively. The experimental and theoretical results are plotted in Figure 3g.

In comparison, the theoretical curve shows a similar trend to the experimental results; the discrepancies can be attributed to the inconsistency of the movement of the actuation frame during the experiments. As indicated by the comparison, the 1DOF expansion of the OPR robot follows the predetermined 1-DOF movement of the origami pattern, which verified the Ori-1DOF movement of the OPR structure. The adjacent blue and black dotted lines in Figure 3e,f are the boundaries of the soft crease, representing the edge of SRTM and LETM, respectively. The dotted lines are always parallel during the 1-DOF expansion, proving that the OPR structure's soft creases only bend without stretching during Ori-1DOF movement.

3.3. Modeling of Exp-DOF Movement

To study the Exp-DOF movement, the model is set up in **Figure 4**a. Here, we assume the robot is driven by only one PDU. The world coordinate system O is established at the center of the origami ball, and the two adjacent LETMs are marked as A and B, respectively, with the local coordinate systems marked. To determine the position, it is assumed that vertex c always lies on the Y axis during the movement. The straight-line distance between points d_A and d_B is the distance between the vertices of the deformed beak-like opening BTD. α_i, β_i, and γ_i ($i = A$, B) denotes the rotation angles of the X, Y, and Z axes of the respective coordinate systems of each LETM.

Points and vectors at the initial position are noted as $\boldsymbol{c}_o$, $\boldsymbol{c}_A$, $\boldsymbol{c}_B$, $\boldsymbol{d}_A$, and $\boldsymbol{d}_B$. And the vectors $\mathbf{c}_A\mathbf{d}_A = \mathbf{d}_A - \mathbf{c}_A$ and $\mathbf{c}_B\mathbf{d}_B = \mathbf{d}_B - \mathbf{c}_B$. The overlapped vector $\mathbf{ce}$ of in coordinate A and B is $\mathbf{c}_A\mathbf{e}_A$ and $\mathbf{c}_B\mathbf{e}_B$, respectively. The rotation matrices that convert the vector in the local coordinate systems to the world coordinate system are

$$\boldsymbol{R}_{\mathrm{AO}} = \mathrm{Rot}(x, g)\mathrm{Rot}(z, h), \quad \boldsymbol{R}_{\mathrm{BO}} = \mathrm{Rot}(x, g)\mathrm{Rot}(z, -h) \tag{6}$$

where g and h indicate the transformation angle around X and Z axis respectively from local to world coordinate system. The ending letter of the subscript of letter denotes coordinate system. The rotation matrices of the coordinate relationship before and after the rotation of the plates A and B are denoted as $\boldsymbol{R}_A$ and $\boldsymbol{R}_B$, which are

$$\mathbf{R}_i = \mathrm{Rot}(z, \gamma_i)\mathrm{Rot}(y, \beta_i)\mathrm{Rot}(x, \alpha_i), \quad i = A, B \tag{7}$$

Thus, the vectors in the world coordinate system after transformation are calculated from Equation (6) and (7) as

$$\mathbf{c}_{\mathrm{AO}}\mathbf{e}'_{\mathrm{AO}} = \mathbf{R}_A \cdot \mathbf{R}_{\mathrm{AO}} \cdot \mathbf{c}_A\mathbf{e}_A, \quad \mathbf{c}_{\mathrm{BO}}\mathbf{e}'_{\mathrm{BO}} = \mathbf{R}_B \cdot \mathbf{R}_{\mathrm{BO}} \cdot \mathbf{c}_B\mathbf{e}_B \tag{8}$$

$$\mathbf{c}_{\mathrm{AO}}\mathbf{d}'_{\mathrm{AO}} = \mathbf{R}_A \cdot \mathbf{R}_{\mathrm{AO}} \cdot \mathbf{c}_A\mathbf{d}_A, \quad \mathbf{c}_{\mathrm{BO}}\mathbf{d}'_{\mathrm{BO}} = \mathbf{R}_B \cdot \mathbf{R}_{\mathrm{BO}} \cdot \mathbf{c}_B\mathbf{d}_B \tag{9}$$

The normal vector of A is $\mathbf{n} = (0, -1, 0)$. In accordance with projection law, the projected vector of $\mathbf{c}_{iO}\mathbf{e}_{iO}$ to plane XOY (i.e., plane XOY is an standardrized expression in the fields of mechanism and robotics, which stands for the plane of Axis X, Axis Y, and there intersection O)

$$\mathbf{p}_{\mathbf{c}_A\mathbf{e}_A} = \mathbf{c}_{\mathrm{AO}}\mathbf{e}_{\mathrm{AO'}} - (\mathbf{c}_{\mathrm{AO}}\mathbf{e}_{\mathrm{AO'}} \cdot \mathbf{n})\mathbf{n} \tag{10}$$

Similarly, $\mathbf{p}_{\mathbf{c_B e_B}}$ can be obtained. Thus, the angle between the projected vectors is

$$\delta = \arccos\left(\frac{\mathbf{p}_{\mathbf{c_A e_A}} \cdot \mathbf{p}_{\mathbf{c_B e_B}}}{|\mathbf{p}_{\mathbf{c_A e_A}}||\mathbf{p}_{\mathbf{c_B e_B}}|}\right) \tag{11}$$

To calculate BTD, the coordinates of d_{AO} and d_{BO} are calculated as following

$$d_{AO'} = \mathbf{c_{AO}d_{AO'}} + c_{AO}, \quad d_{BO'} = \mathbf{c_{BO}d_{BO'}} + c_{BO} \tag{12}$$

Assuming that c_{AO} remains fixed, then $c_{AO} = c_O$. Due to the soft crease bends and stretches, c_{BO} does not coincide with c_{AO}. Dislocation occurs as shown in Figure 4c, with c_{AO} positioned slightly lower than c_{BO}. Then, c_{AO} needs to move forward $\mathbf{u} = [0, \Delta y, 0]^{\mathrm{T}}$ on the Y axis, $c_{AO} = c_O + \mathbf{u}$. The theoretical BTD is calculated as

$$\mathrm{BTD} = \overline{d_{A'}d_{B'}} = |d_{AO'} - d_{BO'}| \tag{13}$$

Experiments are carried out to verify the theoretical results. The opened chamber OPR structure is used to show the deformations of the soft creases more clearly as shown in Figure 4d. The IMU sensors are installed on two adjacent LETMs to measure the rotation angle α_i, β_i, and γ_i. The edges of the two LETMs to be projected are marked with black dotted lines shown in

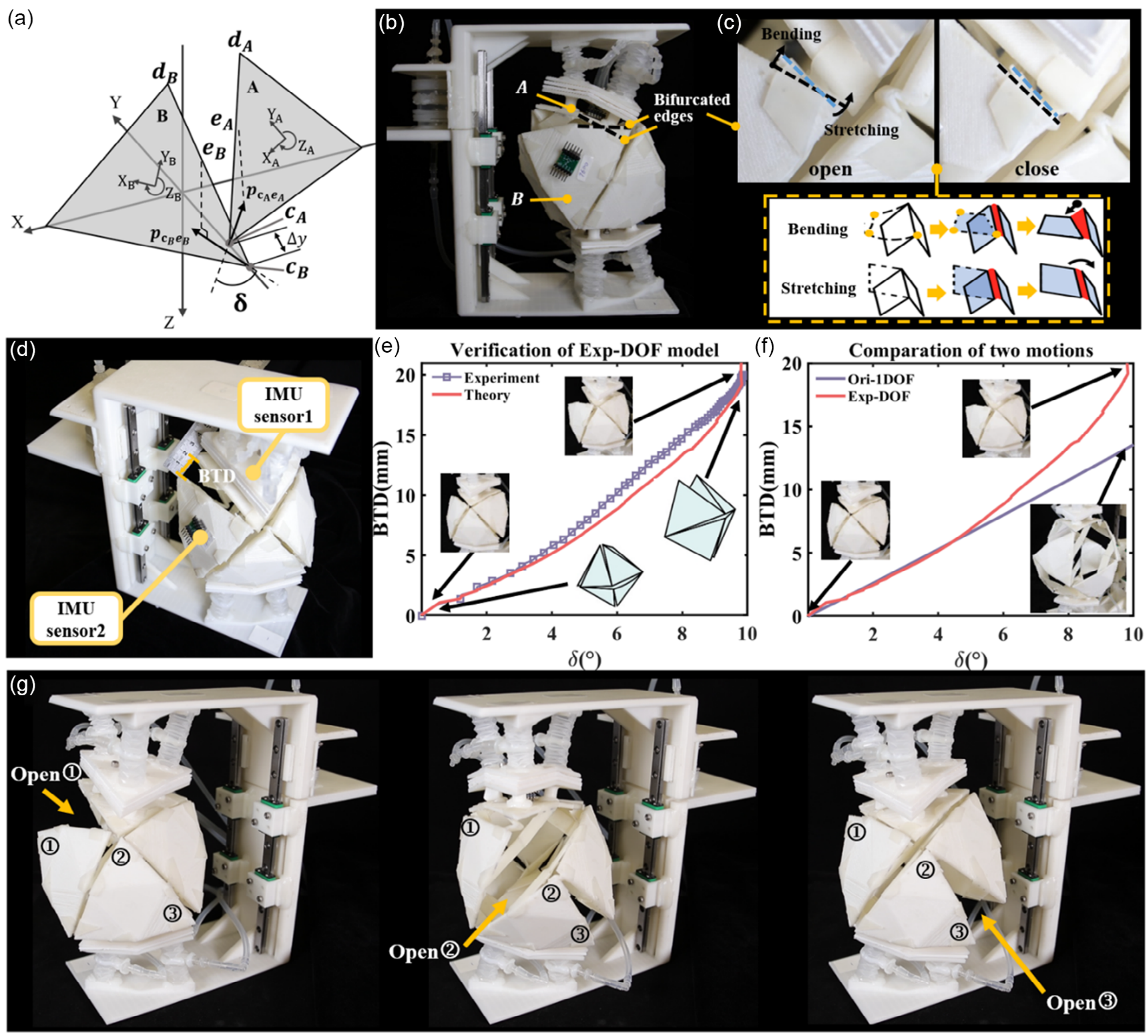

Figure 4. Modeling and verification of the OPR expanded (Exp-DOF) movements due to bifurcation. a) Schematic of Exp-DOF movement. b) Motion of opening a single beak and edges to be projected. c) Details of bifurcation and dislocation of LETMs, indicating the soft creases with both stretching and bending deformations. d) Experiment setup of Exp-DOF movement validation. e) Experiment and theoretical results of Exp-DOF movement validate the modeling of Exp-DOF movement. f) Comparison of Ori-1DOF and Exp-DOF movement using the models. g) Due to the bifurcated multiple Exp-DOF movements, the beak can be opened at multiple locations. j, k, and l indicate different beaks of the OPR robot.

Figure 4b. The distance BTD is calculated from the pixel length during the movement, verified by the maximum distance of 0 mm measured by the ruler. The experimental and theoretical relationship between δ and BTD are plotted in Figure 4e. The two curves show similar trends and small disparities, which verifies the model.

OPR Ori-1DOF and Exp-DOF movement are compared. According to the research of Yang et al.[42] during the Ori-1DOF movement, the relationship of angle δ and the theoretical value of BTD can be given by the formula $\cos\delta = 1 - \frac{1}{2}\overline{d_{A'}d_{B'}}^2$. The BTD in the Ori-1DOF and Exp-DOF movements are plotted in Figure 4f. It is obvious that the change of the BTD during Exp-DOF movement presents a nonlinear trend with an increasing slope while the curve of the Ori-1DOF remains linear, indicating a clear difference between the two kinds of movements.

A practical manifestation of the OPR structural behavior during Exp-DOF movement is shown in Figure 4c. In the contracted state, the blue dotted line is parallel to the black dotted line, while in the expanded state, the two lines intersect. This phenomenon shows that the soft creases stretch and twist during the movement in addition to bending, which is different from the Ori-1DOF movement. It also reflects that the OPR method enables the soft creases to undergo two different movements simultaneously, thereby expanding the DOF of the robot.

Additionally, the OPR robot under Exp-DOF movement in the experiments is only driven by a single PDU while the other maintains undeformed with input pressure fixed. If both sides of PDUs are activated, a larger BTD can be derived. Multiple tests show that the PDU directly connected to the component LETM of the beak contributes the most to the BTD, while the other serves a supportive role. By controlling the PDUs, different beaks can be opened as presented in Figure 4g. The BTDs are measured at about 30 mm, which is 10 mm larger than the single PDU actuation case. Combined with the characteristics of the SDU and PDU, the rotation angle of LETM can be calculated according to the required BTD, and the target air pressure can be obtained for the control of OPR robot.

4. Actuation and Control of OPR Robot

4.1. Driving Units

The contracted, original, and elongated state of SDU is shown in **Figure 5**a. The displacement and pressure relationship of SDU is measured repetitively and plotted in Figure 5b. Its controllable range is about 60 mm. An IMU is attached to the top center of an LETM, and a coordinate system is established, as shown in Figure 5c. By controlling the air pressure of the three SOAs to generate rotation and translations in a single axis, the rotation angles and displacement of the PDU in three directions are recorded and plotted in Figure 5d–f, respectively. The deflection angle of the PDU range on the X and Y axes is about ±15°, and the displacement length on the Z axis ranges from −10 to 5 mm.

4.2. Control System

Figure 6a shows the pneumatic control system consists of two pumps (KVP8S, Kamoer Inc.), two air tanks, a set of solenoid valves (OST Inc.), two MCUs of STM32F103 (ST Microelectronics Inc.), and pressure sensors (XGZP6847A, CFSensor Inc.). PDU and SDUs are controlled by the pneumatic control system. The chamber of the OPR robot is not deflated or inflated by the system but driven by SDU and PDUs. Figure 6b is the control scheme of the system. A pressure feedback loop is set up to control the pressure. The air pressure sensors are used to collect the actual air pressure, and the serial port is used to give the target pressure. According to the comparison result between the actual and target pressure values given by the serial port, two MCUs give commands to the pumps or valves, respectively.

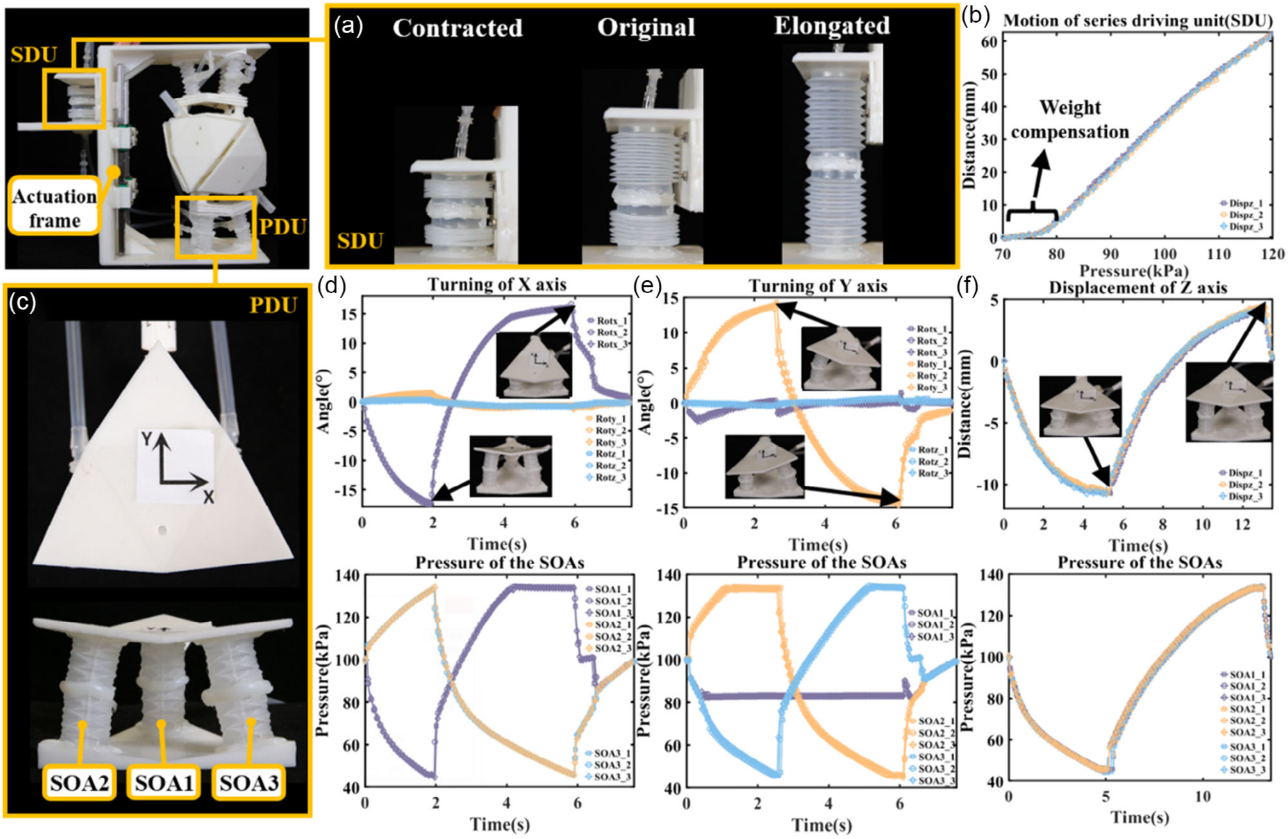

Figure 5. Pneumatic actuation frame and control. a) The contracted, original, and elongated state of series-driving unit (SDU). b) The displacement and pressure relationship of SDU, which has a weight compensation at the beginning. c) Structure and coordinate system of parallel-driving unit (PDU). d) Turning angle on axis X and given pressure of SOAs. Rotx, Roty, and Rotz stand for the turning angle on X, Y, and Z axis, respectively. The test has been conducted three times, which were noted as, for example, from Rotx_1 to Rotx_3. e) Turning angle on axis Y and given pressure of SOAs. f) Displacement of axis Z and given pressure of SOAs.

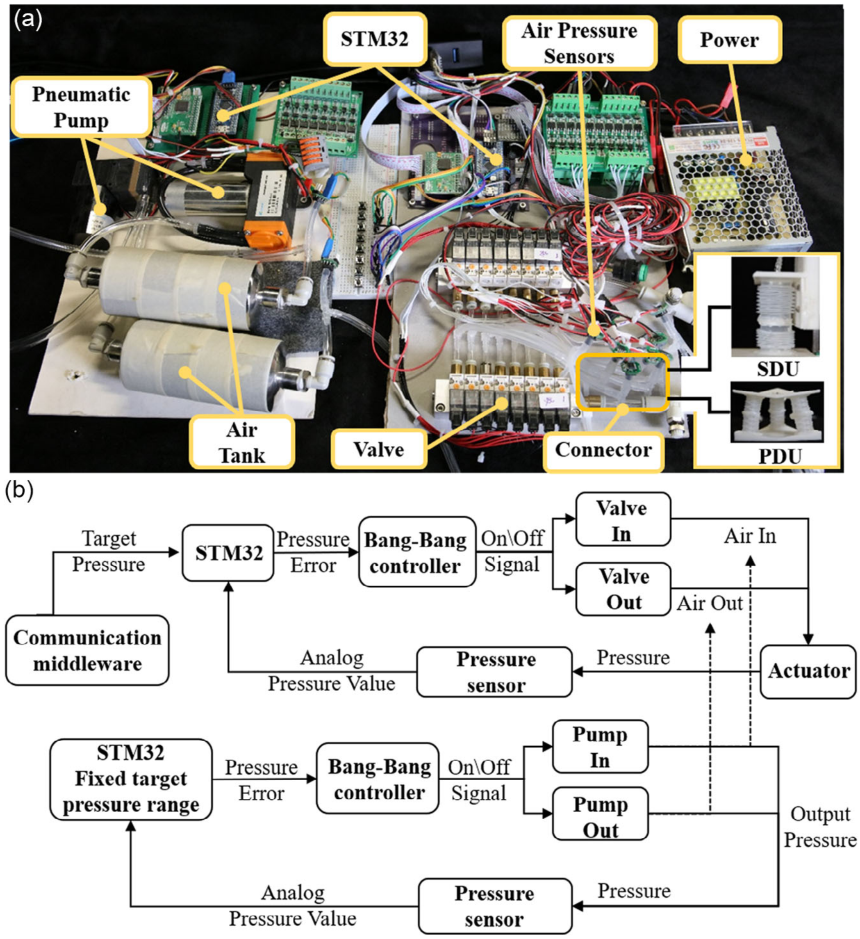

Figure 6. a) The pneumatic actuation hardware and air circuit of connection with the driving units, which is noted with the black line. b) The control logic of the actuation.

The valves open or close the pneumatic channels connected to the actuators to reach a certain pressure. The pumps are controlled by a similar feedback logic to work intermittently to give the output pressure within a certain range, and the output air pressure before passing the valve is collected for feedback. A range limitation provides a smaller pressure difference between the air source and the SOAs to smooth the movement of the robot.

5. OPR Soft Robots

5.1. Multifunctional OPR Gripper

The open-chamber OPR structure driven by the actuation frame is applied as a multifunctional soft robotic gripper. By regulating the PDUs, the multifunctional gripper achieves unilateral clamping in any of the six directions. The gripper can carry out grasping activities in two modes: the grip and the swallow. By regulating the SDUs, the six openings of the gripper simultaneously open and close, allowing the moving target object to enter. Thus, the gripper can capture aquatic life by enclosing the chamber when working underwater.

In the grip mode, three main steps are shown in **Figure 7**a, the tips of the gripper is composed by SRTMs. The attached silicone contacts the target object, providing friction during the grasping. In the swallow mode, as shown in Figure 7b, two selected beaks and the volume of the ball are used. Beak 1 opens to pick up the orange and then closes to swallow. The orange adjusts positions within the chamber according to the tilt pose of the gripper. Once Beak 2 opens, the orange is released to the destination. The advantage of gripping with Exp-DOF movement is that it can decrease the aiming and position adjustment difficulty caused by the large size variation under Ori-1DOF movement. If the gripper is connected to a robot arm, the necessity of the arm traveling a significant distance to offset the size variation is eliminated, which makes positioning for gripping simpler.

For the circumstance of working underwater, the enclosed capture of a motorized fish toy is shown in Figure 7c. The fish swims in the water randomly. The six openings of the chamber allow the fish to enter when the SDU is elongated. Once the fish swims inside the chamber, the SDU contracts, and the fish is enclosed in the chamber without clamping by the rigid components, demonstrating the potential for sampling fragile aquatic organisms. In addition, the gripper can grip objects underwater

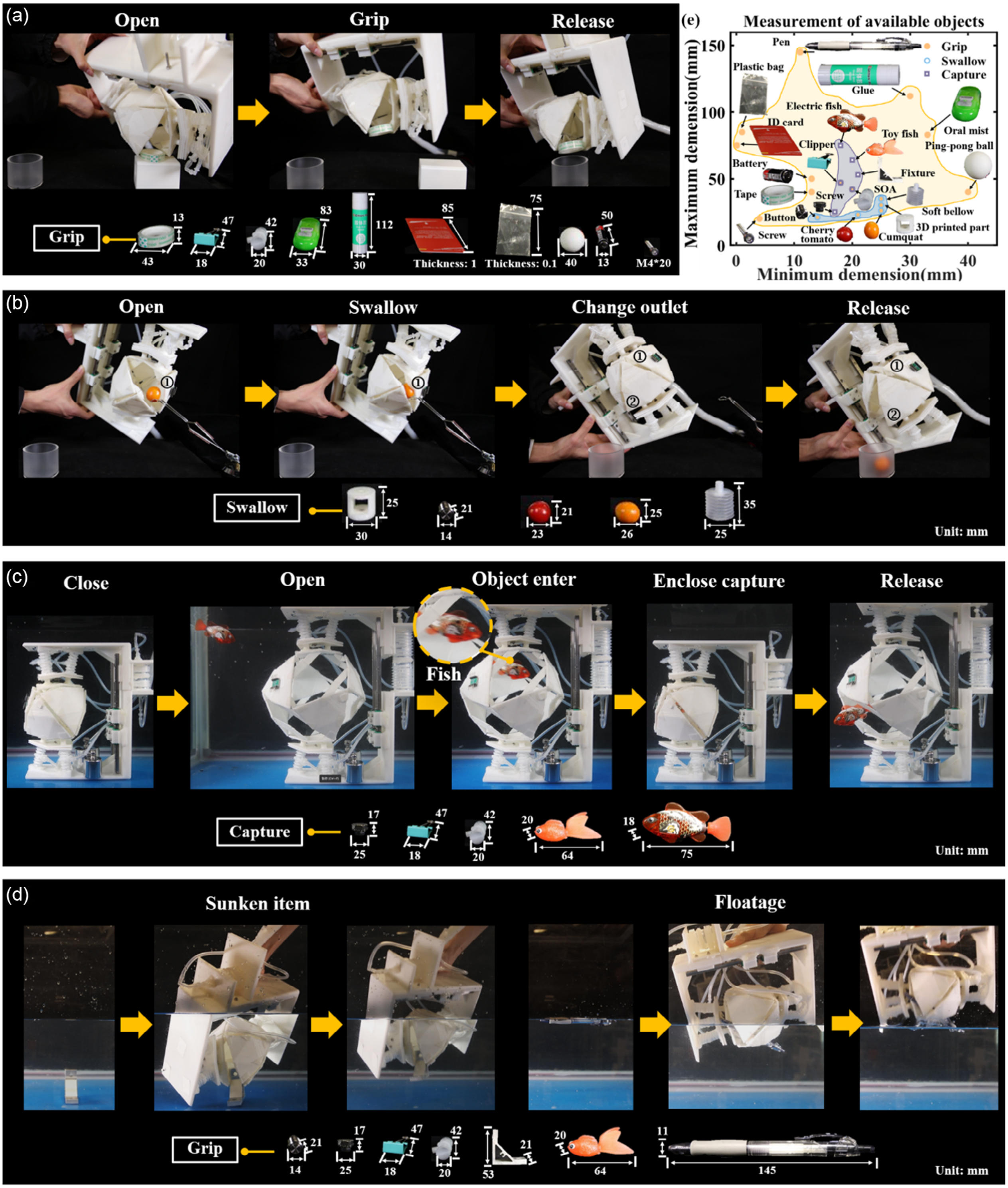

Figure 7. The multifunctional OPR gripper. a) Steps of gripping by the OPR gripper and the dimensions of the objects that can be picked up. b) Steps of swallowing and the dimensions of the objects that can be swallowed. The unit of dimension is millimeters (mm). j and k indicate the different beaks of the OPR robot. c) Steps of enclose capturing a swimming object, namely, a motorized fish toy. d) Steps of gripping sunken items and floatage in the water. e) Maximum and minimum dimensions of available objects for grip, swallow, and capture are compared. The objects that can be swallowed are rounded in profile, i.e., the difference between the maximum and minimum dimensions are small, with maximum dimensions smaller than 35 mm. The minimum dimensions of the objects that can be picked up are smaller than 40 mm.

with its beak. As shown in Figure 7d, it is easy to grasp both the sunken items and the floatage with movements of bifurcation. When gripping floating objects, the gripping points are positioned farther apart compared to desktop tasks, which allow longer floatage to be grasped, such as pens.

The objects that can be grasped by the gripper are plotted with maximum and minimum dimensions as shown in Figure 7e. In the experiments of grip mode, a variety of objects are picked from the original location and placed at the destination, including small screws (M4), thin cards, ping-pong balls, and freshness protection packages. A certain beak is used in this mode, and the minimum dimensions of the suitable objects are smaller than 40 mm. The tested objects that can be swallowed are smaller than 35 mm. These objects are rounded in profile, i.e., the difference between the maximum and minimum dimensions is small for them to be swallowed. The OPR gripper with swallow mode has the potential for applications such as fruit harvesting from the crop. As the gripper can grip in six directions, it provides a new way of pick-and-place that alleviates the need for distal adjusting of the robotic arm it is mounted on.

5.2. OPR Pump

A soft robotic pump with a closed OPR chamber for fluid transportation is proposed and tested in setup as shown in **Figure 8**a. Utilizing the OPR structure with an airtight chamber, the OPR fluid pump configuration, connection of tubes, and labeling of the SOAs are shown in Figure 8b. Two silicone-injected soft tubes (T1) with 8 mm diameter made of Eco-flex 30 are installed on the symmetric sides of the OPR chamber and sealed with soft silicone glue. Tube T1 can be clamped by SRTMs and blocked for airtightness. Tube T2 connected with T1 is of higher hardness and capable of keeping itself open when the pump works.

Combining the actuations of SDU and PDUs, the pump can achieve fluid transportation following the workflow of inhaling and exhaling as shown in Figure 8c. The workflow is divided into five states denoted as S1–S5. In the half cycle of inhaling (S2, S3), for the fluid to enter from the inlet, SOAs 2 and 5 contract while SOAs 1, 3, 4, and 6 elongate to open the inlet side of the beak and keep the outlet side clamped. The opening of the inlet can be seen in the solid frame in addition to S2. To absorb fluid, the SDU is inflated to the maximum elongation state (S3), and the volume of the chamber increases to create a negative pressure.

In the consequent half cycle of exhaling (S4, S5), at the maximum elongation of SDU (S4), SOAs 1, 2, 5, and 6 are elongated while SOAs 3 and 4 are contracted simultaneously to clamp the originally opened inlet tube and open the opposite outlet. To pump the fluid out (S5), the SDU contracts to decrease the volume of the chamber, and a positive pressure is formed inside relative to the ambient. The exhaling stops when the volume reaches the minimum, and the OPR pump returns to the reset state (S1).

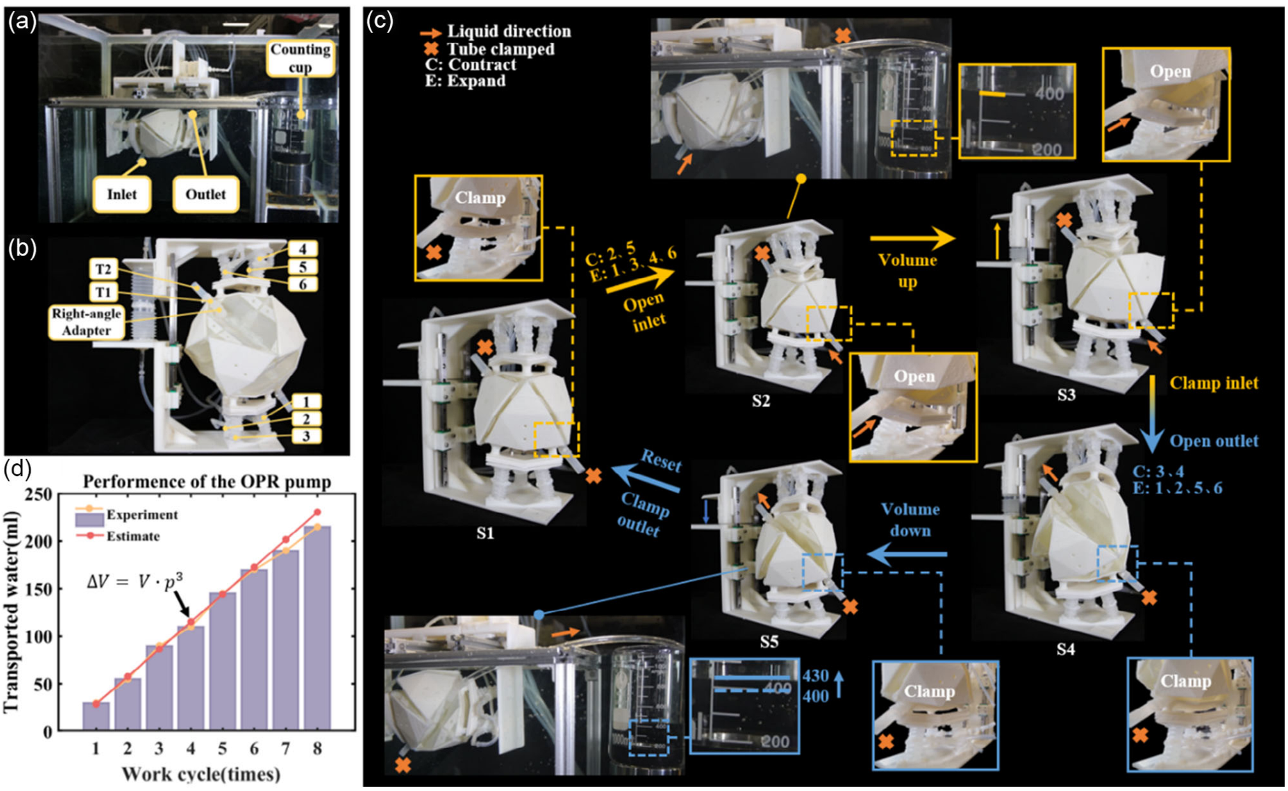

Figure 8. The demonstration of the OPR pump. a) Experiment setup of fluid transportation. b) Optimized soft tubes of OPR pump, i.e., tube T1 can be clamped by SRTMs and blocked for airtightness, tube T2 connected with T1 are of higher hardness and capable of keeping itself opened when the pump is working. The SOAs are marked. c) Fluid transportation workflow of inhaling and exhaling. d) The small disparities between the actual transported and estimated volume by the pump validate the practicality of the OPR pump for fluid transportation in the selected direction.

Cycling the inhaling and exhaling processes, continuous fluid transportation can be achieved. In the experiment, the pump is submerged in the water, the outlet tube is extended into the counting cup where the water level is recorded as shown in Figure 8a. The water was pumped out from the aquarium into the counting cup. The water level in the cup rises obviously as shown in Figure 8c. In 1 cycle, around 30 mL water is pumped out, and the level in the cup rises from 400 mL to 430 mL. The volume difference of the closed OPR chamber between the expanded and contracted states of the Ori-1DOF movement is calculated as $V = 450$ mL. In the experiment, the actual elongated length of SDU is around $p = 2/5$ of the fully expanded length. Thus, the pumped-out water $\Delta\mathbf{V}$ in each cycle can be estimated by the following equation:

$$\Delta\mathbf{V} = \mathbf{V} \cdot \mathbf{p}^3 \tag{14}$$

which is about 28.8 mL. The experimental and estimated results are plotted in Figure 8d. The small disparities between the actual transported and estimated volume by the pump validate the practicality of the OPR pump for fluid transportation in the selected direction. In addition, the inlet and outlet silicone soft tubes can be installed in any two of the six openings. With appropriate actuation, the direction of the fluid in and out can be reversed during work. The OPR pump integrates the pump and the valve without electronic components, which significantly reduces the complexity of the system.

6. Conclusion

In this work, the OPR method is proposed, inspired by the multi-DOF volume-regulating movements of the fluid-transportation organs, to apply rigid origami mechanism on the hyperelastic chamber for obtaining controllable multi-DOF motions and expanding functionality. By attaching a set of rigid modules according to the cuboctahedron origami ball to the soft chamber for rigidification, the resultant OPR structure retains the predetermined 1-DOF movement of the rigid origami mechanism and expands to the bifurcated movements due to the soft–rigid characteristics.

By analyzing the deformation of the soft creases and considering the rigid origami kinematics, the kinematic models of the predetermined and the expanded movements are derived. The model of the Ori-1DOF movement considers only the bending of the soft crease, while the Exp-DOF model considers simultaneous stretching and bending. The model predicts the relationship between the rotational angle of the adjacent LETM plates and the distance of the beak-like opening. The existence of two different movements and the correctness of models are verified by experiments. Driven by two sets of actuation units, two OPR soft robots, including a multifunctional gripper and a pump, are developed. Enabled by the Exp-DOF, the gripper obtained a swallow mode and is able to capture objects underwater. The pump shows the feasibility of fluid transportation without electronic components. Thus, the practicality of OPR to regulate chamber deformation and generate new functions for soft robots is proved.

In future work, the actuation frame of the OPR robot can be further simplified with driven units reduced and integrated inside the chamber. The motion range of the robot can be significantly enlarged by increasing the range of the driving units that further stretch the soft creases.

Supporting Information

Supporting Information is available from the Wiley Online Library or from the author.

Acknowledgements

D.L. and S.L. equally contributed to this work. This work was partly supported by the National Key R&D Program of China (grant no. 2022YFB4701200), Shenzhen Science and Technology Program (grant nos. JCYJ20220530114615034 and JCYJ20220818100417038), and Guangdong Basic and Applied Basic Research Foundation (grant no. 2021A1515110658).

Conflict of Interest

The authors declare no conflict of interest.

Data Availability Statement

The data that support the findings of this study are available in the supplementary material of this article.

Keywords

origami, soft robots, soft-rigid bifurcations

Received: November 14, 2023
Revised: January 23, 2024
Published online: March 14, 2024

[1] A. J. Cummins, *Am. J. Dig. Dis.* **1958**, *3*, 710.
[2] N. H. Cohrs, A. Petrou, M. Loepfe, M. Yliruka, C. M. Schumacher, A. X. Kohll, C. T. Starck, M. Schmid Daners, M. Meboldt, V. Falk, W. J. Stark, *Artif. Organs* **2017**, *41*, 948.
[3] A. X. Kohll, N. H. Cohrs, R. Walker, A. Petrou, M. Loepfe, M. Schmid Daners, V. Falk, M. Meboldt, W. J. Stark, *Soft Rob.* **2018**, *6*, 206.
[4] G. Torregrossa, A. Anyanwu, F. Zucchetta, G. Gerosa, *Ann. Cardiothorac. Surg.* **2014**, *3*, 612.
[5] W. E. Cohn, D. L. Timms, O. H. Frazier, *Nat. Rev. Cardiol.* **2015**, *12*, 609.
[6] Y. Sawa, G. Matsumiya, S. Miyagawa, E. Tatsumi, T. Abe, K. Fukunaga, S. Ichiba, T. Taguchi, K. Kokubo, T. Masuzawa, A. Myoui, M. Nishimura, T. Nishimura, T. Nishinaka, E. Okamoto, S. Tokunaga, T. Tomo, T. Tsukiya, Y. Yagi, T. Yamaoka, *J. Artif. Organs* **2020**, *23*, 1.
[7] Q. Tan, Y. Chen, J. Liu, K. Zou, J. Yi, S. Liu, Z. Wang, *Front Rob. AI* **2021**, *8*, 688697.
[8] P. Z. Zhang, Q. C. Wang, M. Kamezaki, Z. Y. He, Y. Iwamoto, Y. Ido, H. Sakamoto, S. Sugano, in *IEEE ASME Int. Conf. Advanced Intelligent Mechatronics*, Sapporo, Japan, July **2022**, pp. 1115–1120.
[9] C. Christianson, Y. Cui, M. Ishida, X. B. Bi, Q. Zhu, G. Pawlak, M. T. Tolley, *Bioinspiration Biomimetics* **2020**, *16*, 016014.

[10] J. Davies, M. T. Thai, H. Low, P. T. Phan, T. T. Hoang, N. H. Lovell, T. N. Do, *Soft Rob.* **2023**, *10*, 1055.
[11] S. Liu, W. Lv, Y. Chen, G. Lu, *J. Mech. Rob.* **2016**, *8*, 031002.
[12] M. Meloni, J. Cai, Q. Zhang, D. Sang-Hoon Lee, M. Li, R. Ma, T. E. Parashkevov, J. Feng, *Adv. Sci.* **2021**, *8*, 2000636.
[13] D. Rus, M. T. Tolley, *Nat. Rev. Mater.* **2018**, *3*, 101.
[14] D. Li, E. Q. Yumbla, A. Olivas, T. Sugar, H. B. Amor, H. Lee, W. Zhang, D. M. Aukes, *IEEE/ASME Trans. Mechatron.* **2022**, *28*, 1466.
[15] S. Liu, Z. Fang, J. Liu, K. Tang, J. Luo, J. Yi, X. Hu, Z. Wang, *Front. Rob. AI* **2021**, *8*, 614623.
[16] A. L. Shoushtari, G. A. Naselli, A. Sadeghi, B. Mazzolai, in *IEEE Int. Conf. Robot*, Montreal, QC, Canada, May **2019**, pp. 7415–7420.
[17] Y. Liu, L. Yang, Y. Sun, presented at *2022 Int. Conf. on Sensing, Measurement & Data Analytics in the era of Artificial Intelligence (ICSMD)*, Harbin, China, November–December **2022**, pp. 1–6.
[18] M. Mete, J. Paik, *IEEE Rob. Autom. Lett.* **2021**, *6*, 8213.
[19] S. Liu, J. Liu, K. Zou, X. Wang, Z. Fang, J. Yi, Z. Wang, *J. Mech. Rob.* **2022**, *14*, 060912.
[20] M. Park, W. Kim, S. Y. Yu, J. Cho, W. Kang, J. Byun, U. Jeong, K. J. Cho, *IEEE Rob. Autom. Lett.* **2023**, *8*, 864.
[21] C. J. Cai, X. Xiao, M. S. Kalairaj, I. J. J. Lee, A. K. Mugilvannan, B. S. Yeow, J. H. Tan, H. Huang, H. L. Ren, *IEEE-ASME T Mech.* **2021**, *26*, 1678.
[22] T. Jin, L. Li, T. Wang, G. Wang, J. Cai, Y. Tian, Q. Zhang, *IEEE Trans. Rob.* **2022**, *38*, 748.
[23] S. Yuan, S. Cao, J. Xue, S. Su, J. Yan, M. Wang, W. Yue, S. S. Cheng, J. Liu, J. Wang, S. Song, M. Q. H. Meng, H. Ren, *IEEE Rob. Autom. Lett.* **2022**, *7*, 10486.
[24] Z. C. Kan, Y. Z. Zhang, Y. Yang, Y. A. Tse, M. Y. Wang, in *2019 2nd IEEE Int. Conf. on Soft Robotics (Robosoft 2019)*, Seoul, Korea (South), April **2019**, p. 470–476.
[25] S. Li, J. J. Stampfli, H. J. Xu, E. Malkin, E. V. Diaz, D. Rus, R. J. Wood, presented at *IEEE Int. Conf. Robot*, 2019.
[26] Z. Yang, D. Chen, D. J. Levine, C. Sung, *IEEE Rob. Autom. Lett.* **2021**, *6*, 7145.
[27] Y. Kim, Y. Cha, *Front. Bioeng. Biotechnol.* **2020**, *8*, 461.
[28] J. Li, H. Godaba, Z. Q. Zhang, C. C. Foo, J. Zhu, *Extreme Mech. Lett.* **2018**, *24*, 30.
[29] X. Zou, T. Liang, M. Yang, C. LoPresti, S. Shukla, M. Akin, B. T. Weil, S. Hoque, E. Gruber, A. D. Mazzeo, *Soft Rob.* **2022**, *9*, 542.
[30] R. Wang, Y. Song, J. S. Dai, *Mech. Mach. Theory* **2021**, *161*, 104245.
[31] Z. Tang, K. Wang, E. Spyrakos-Papastavridis, J. S. Dai, *J. Mech. Rob.* **2022**, *14*, 060907.
[32] S. Mintchev, J. Shintake, D. Floreano, *Sci. Robot.* **2018**, *3*, aau0275.
[33] J. A. Faber, A. F. Arrieta, A. R. Studart, *Science* **2018**, *359*, 1386.
[34] H. Zhang, *IEEE/ASME Trans. Mechatron.* **2022**, *27*, 2589.
[35] Y. Zhu, E. T. Filipov, *Proc. Math. Phys. Eng. Sci.* **2019**, *475*, 20190366.
[36] K. Zhang, Y. Zhu, C. Lou, P. Zheng, M. Kovac, in *2019 2nd IEEE Int. Conf. on Soft Robotics (Robosoft 2019)*, Seoul, Korea (South), April **2019**, pp. 821–827.
[37] T. Amadeo, D. Van Lewen, T. Janke, T. Ranzani, A. Devaiah, U. Upadhyay, S. Russo, *Front Rob. AI* **2021**, *8*, 731010.
[38] C. Zhang, Z. Zhang, Y. Peng, Y. Zhang, S. An, Y. Wang, Z. Zhai, Y. Xu, H. Jiang, *Nat. Commun.* **2023**, *14*, 4329.
[39] B. Zhang, P. Yang, X. Gu, H. Liao, *IEEE Rob. Autom. Lett.* **2021**, *6*, 7736.
[40] Z. E. Teoh, B. T. Phillips, K. P. Becker, G. Whittredge, J. C. Weaver, C. Hoberman, D. F. Gruber, R. J. Wood, *Sci. Rob.* **2018**, *3*, eaat5276.
[41] Q. Xia, L. Xu, C. Liu, Y. Yang, Y. Chen, S. Zhang, C. Yang, *Adv. Eng. Mater.* **2023**, *25*, 2201416.
[42] F. Yang, Z. You, Y. Chen, *Mech. Mach. Theory* **2020**, *145*, 103698.
[43] S. Liu, Y. Zhu, Z. Zhang, Z. Fang, J. Tan, J. Peng, C. Song, H. H. Asada, Z. Wang, *IEEE/ASME Trans. Mechatron.* **2020**, *26*, 2747.
[44] D. Koks, in *Explorations in Mathematical Physics: The Concepts Behind an Elegant Language*, Springer, New York **2006**.